ADVANCED HEALTHCARE MATERIALS
www.advhealthmat.de

Biofabrication and Monitoring of a 3D Printed Skin Model for Melanoma

Paula Vázquez-Aristizabal, Malou Henriksen-Lacey, Clara García-Astrain, Dorleta Jimenez de Aberasturi, Judith Langer, Claudia Epelde, Lucio Litti, Luis M. Liz-Marzán, and Ander Izeta**

There is an unmet need for in vitro cancer models that emulate the complexity of human tissues. 3D-printed solid tumor micromodels based on decellularized extracellular matrices (dECMs) recreate the biomolecule-rich matrix of native tissue. Herein a 3D in vitro metastatic melanoma model that is amenable for drug screening purposes and recapitulates features of both the tumor and the skin microenvironment is described. Epidermal, basement membrane, and dermal biocompatible inks are prepared by means of combined chemical, mechanical, and enzymatic processes. Bioink printability is confirmed by rheological assessment and bioprinting, and bioinks are subsequently combined with melanoma cells and dermal fibroblasts to build complex 3D melanoma models. Cells are tracked by confocal microscopy and surface-enhanced Raman spectroscopy (SERS) mapping. Printed dECMs and cell tracking allow modeling of the initial steps of metastatic disease, and may be used to better understand melanoma cell behavior and response to drugs.

1. Introduction

Malignant melanoma (MM) is a neoplasia that metastasizes rapidly and is often underdiagnosed, becoming a life-threatening skin tumor.[1] It is also one of the most common cancers in young adults; hence, understanding the mechanisms of invasion and immune evasion is key to developing improved therapies for MM.[2–4] A number of high-throughput in vitro tumor models have been created to study the reactions of tumors against novel drug candidates. However, many drugs under development present inconsistent effects between preclinical and clinical stages,[5,6] resulting in high drug attrition rates. Of note, cancer cell behavior is highly dependent on adjacent cell populations and other components of the tumor

P. Vázquez-Aristizabal, A. Izeta
Stem Cells and Aging Group
Biogipuzkoa Health Research Institute
Paseo Dr. Begiristain s/n, Donostia-San Sebastián 20014, Spain
E-mail: ander.izetapermisan@osakidetza.eus

P. Vázquez-Aristizabal, M. Henriksen-Lacey, C. García-Astrain, D. Jimenez de Aberasturi, J. Langer, L. M. Liz-Marzán
CIC biomaGUNE
Basque Research and Technology Alliance (BRTA)
Paseo de Miramón 194, Donostia-San Sebastián 20014, Spain
E-mail: llizmarzan@cicbiomagune.es

M. Henriksen-Lacey, C. García-Astrain, D. Jimenez de Aberasturi, J. Langer, L. M. Liz-Marzán
Centro de Investigación Biomédica en Red
Bioingeniería
Biomateriales y Nanomedicina (CIBER-BBN)
Donostia-San Sebastián 20014, Spain

D. Jimenez de Aberasturi, L. M. Liz-Marzán
Ikerbasque Basque Foundation for Science
Bilbao 48009, Spain

C. Epelde
Obstetrics and Gynaecology Service
Donostia University Hospital
Paseo Dr. Begiristain s/n, Donostia-San Sebastián 20014, Spain

L. Litti
Department of Chemical Sciences
University of Padova
Via Marzolo, 1, Padova 35131, Italy

L. M. Liz-Marzán
Cinbio
Universidade de Vigo
Campus Universitario
Vigo 36310, Spain

A. Izeta
School of Engineering
Tecnun-University of Navarra
Donostia-San Sebastián 20009, Spain

The ORCID identification number(s) for the author(s) of this article can be found under https://doi.org/10.1002/adhm.202401136

DOI: 10.1002/adhm.202401136

microenvironment, which in turn will affect therapeutic effectiveness of anticancer drugs. Current in vitro models based on tumorigenic cell monolayers do not properly replicate tumor biology, and the 3D tumor microenvironment must be considered.

3D models (such as spheroids or 3D printed hydrogels) better mimic the interplay between the extracellular matrix (ECM) and cancerous and stromal cells in real tissues.[7,8] They present the additional advantage of (similar to in vivo tumors) including quiescent, apoptotic, proliferating, and hypoxic cells.[2,9] Nonetheless, although the clinical importance of metastasis in MM is well known, available in vitro models have limitations to mimic the transition from premetastatic to metastatic niches.[10–12] To overcome these limitations, researchers have turned to 3D bioprinting technology for the fabrication of more realistic models of skin and melanoma, as the inherently layered structure of skin makes it particularly suitable for reproduction through layer-by-layer deposition. Additionally, 3D bioprinting offers several advantages over traditional fabrication techniques like electrospinning, casting, and molding. These include precise control over tissue shape and depth, versatile bioink composition, and the ability to use multiple materials for greater customization.[13] Its biocompatibility enables direct cell incorporation, and it allows precise placement of different cell populations, enhancing tissue functionality and complexity. Currently, extensive research is focused on 3D printing skin models that incorporate pigment cells, vascularization, or immune cells.[14–17] Ideally, new models should also allow for the monitoring of cellular traits (such as tumor cell proliferation, migration, and metastasis) during prolonged periods.[18,19] To accommodate most of the pending issues in MM in vitro model development, the use of well-designed biomaterial-based scaffolds is crucial.

Aside from natural biomaterials,[11,17] the current ECM gold-standard in 3D model development is Matrigel, a commercial solubilized protein preparation extracted from Engelbreth–Holm–Swarm (EHS) mouse sarcoma. Despite of its wide use, Matrigel presents two relevant shortcomings: i) it varies batch-to-batch in protein composition;[20,21] and ii) depending on diverse settings, it may promote tumor cell differentiation, angiogenesis, and metastasis.[22] Therefore, when modeling tumors the inherent bioactivity of Matrigel may lead to misinterpreted results. On the other hand, tissue-derived ECM is extraordinarily rich in growth factors, proteoglycans, glycoproteins, and signaling molecules.[23] By applying different decellularization techniques, i.e., the elimination of cells from tissues, it is possible to elaborate tissue-specific decellularized ECM (dECM) hydrogels, which can be subsequently used as bioinks.[24,25] In general, dECMs recapitulate the molecular identity of native ECMs with high fidelity.[26] The functionalization of dECMs as bioinks for 3D printing allows layer-by-layer fabrication of constructs with predesigned compositions,[27] thereby broadening their applications in the biomedical field.[28–30]

The understanding of cell dynamics in metastasis requires cell tracking in space and time, which is typically achieved by the use of confocal fluorescence microscopy. However, most of the employed fluorophores present poor lifespan/cytotoxicity ratios.[31,32] Alternatively, Raman mapping can also be used as a bioimaging tool,[33] in which vibrational fingerprints provide quantitative information on the molecular composition of the sample. However, the Raman scattering process is very inefficient and requires large amounts/high concentrations of the analyte for reliable detection. This issue can be resolved by using the so-called surface-enhanced Raman scattering (SERS) technique, which relies on amplification by plasmonic fields near a metallic nanostructure and allows much lower detection limits.[34–36] For SERS bioimaging, typically gold nanostars (AuNSs) or gold nanorods (AuNRs) are encoded with Raman-active molecules (Raman Reporters), resulting in SERS-encoded AuNPs (SERS tags) that can label cells with minimum photodegradation and high biocompatibility. Given the narrow and specific peaks in SERS spectra, libraries of SERS tags can be prepared and multiplex bioimaging may be carried out for extended periods, with no significant loss of the SERS signal.[37,38] Although SERS tags have been extensively employed in 2D cell cultures,[39–41] their application in 3D models is still rare,[42,43] even though it has been reported to enable high-resolution imaging in 3D.[44]

We describe herein a 3D in vitro MM model that is amenable for drug screening purposes and recapitulates features of both the tumor and the skin microenvironments. In pursuit of this goal, we developed three bioinks with suitable rheological properties for 3D printing that mimicked the dermal, epidermal, and basement membrane (BM) compartments of the skin. We utilized porcine skin to source bioinks for dermis and epidermis dECM, whereas human-derived amniotic membrane was used to produce the BM ink. Finally, different combinations of stromal cells plus metastatic and nonmetastatic cells were tested, prelabelled with either fluorophores or SERS tags, to allow their study over time using either confocal laser scanning microscopy (CLSM) or SERS. Importantly, the combination of heterogeneous cell populations and a dECM-based molecule-rich matrix within the microtissue, including a BM component, permitted us to model the initial stages of tumor cell migration through the BM, eventually leading to metastatic disease.

2. Results and Discussion

To more accurately recapitulate the features of malignant melanoma in vitro, a 3D cell model was designed in which the corresponding dECM-based materials, in combination with cells and NPs, were printed into a trilayered structure (**Figure 1**). This model was evaluated using multiple readouts, including migration assays, 3D SERS imaging, and drug testing.

2.1. dECM Ink Preparation and Characterization

Porcine dermis and epidermis, and hAM were subjected to tailored decellularization protocols, as described in the experimental section and in Table S1 (Supporting Information). Porcine skin has many similarities to human skin, including similar thickness, architecture and appendages,[45,46] and various studies have described the use of decellularized porcine skin (acellular patches) for the treatment of diverse tissue defects.[47,48] On the other hand, the composition of human-derived amniotic membrane (hAM) involves different collagens, laminins, and other structural biomolecules found in basement membranes (Figure S1, Supporting Information), and it has been previously used as a basement membrane-like tissue.[49,50] Efficient tissue decellularization is essential to guarantee bioink biocompatibility and

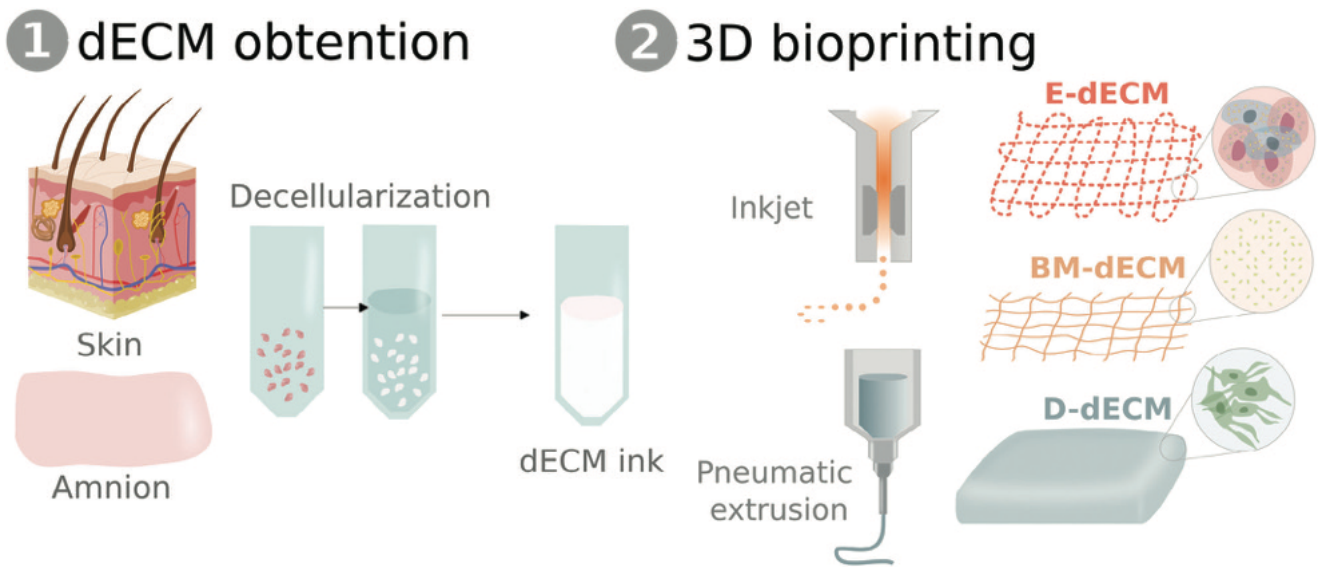

Figure 1. Schematic representation of the biomaterial development process and the fabrication of the 3D printed model.

to enhance tissue-specific functionality upon incorporation of cells. Decellularization efficiency was demonstrated by the absence of cell nuclei in histological sections (**Figure** 2A–1A″), as well as by total DNA quantification (<50 ng DNA mg^{-1} tissue) (Figure 2B–1B″), both of which are commonly used acceptance criteria.[51]

With the aim of creating printable materials, decellularized tissues were freeze-dried and ground into powder. Collagenous tissues were digested under acidic conditions and keratins under basic conditions, until homogeneous solutions were obtained (Figure 2C–1C″). Preinks were neutralized to physiological pH prior to incorporation of cells. We fine-tuned the decellularization process, printability and biocompatibility of three dECM-based materials on the basis of previous reports on the decellularization and formulation of porcine dermis and hAM into hydrogels or extracts.[52–54] Then, to fabricate a 3D microtissue intended to accurately model malignant melanoma and replicate the metastatic process in vitro, two melanoma cell lines (451Lu and WM164) were combined with healthy human dermal fibroblasts. The use of a bioderived matrix allows a better 3D representation of the diseased microenvironment, compared to spheroids or layered models composed of materials such as rat tail collagen or agarose.[12,55]

In terms of mimicking tissues in vitro, commercially available ECMs such as Matrigel are often employed to promote cell migration in a 3D environment, but without considering the overall tissue heterogeneity. Other commercially available kits, usually based on collagen, can also be used to conduct cell invasion assays. The primary motivation for choosing biomaterials is their ease of use; however, both the structural and molecular identity of the tissues should be strictly taken into consideration for in vitro modelling. Hence, we proceeded to print a layered model through the controlled deposition of bioinks, forming a 3D microtissue that could recapitulate both skin architecture and melanoma features. Prior to printing, we carried out a rheological characterization (storage and loss moduli and viscosity) of the bioinks. Additional tests were also conducted to define amplitude and frequency settings for temperature and viscosity assays (Figure S2, Supporting Information). The dermal dECM (D-dECM) showed a gel-like behavior, which is reflected in the storage modulus (G′) being greater than the loss modulus (G″) in the linear viscoelastic region (LVR), both of them independent of frequency. After thermal gelation of D-dECM, both G′ and G″ increased and were stable over time, indicating that further crosslinking was achieved at 37 °C (**Figure** 3A). The shear thinning behavior of the D-dECM ink's viscosity hinted toward printability by pneumatic extrusion (Figure S3A, Supporting Information). The printing assays indeed proved to be reproducible (Figure S3B,D, Supporting Information), with the hydrogel presenting a swelling behavior, reaching a maximum value after 72 hours (Figure S3C,E, Supporting Information). In the case of the amniotic membrane (AM-dECM) ink, similar results were obtained, albeit with a gel behavior being observed over the whole temperature range of 10–40 °C (Figure 3A'). At lower temperatures, G′ and G″ were closer to each other, indicating a more liquid-type behavior, whereas as the temperature increases, crosslinking into a gel is reflected in a gradual separation of the moduli from each other. Based on these findings, we precooled the AM-dECM ink to have a less viscous sample that could be printed by the inkjet technique. This strategy allowed us to deposit a thinner layer that better mimicked the basement layer, as compared to pneumatic extrusion (Figure S3F). On the contrary, the epidermal dECM (E-dECM) behaved as a liquid in the LVR, regardless of temperature (Figure 3A″). For this reason and to ensure the viability of cells included in the ink, the E-dECM was printed by the inkjet technique, using a cell-friendly, drop-on-demand strategy. Finally, despite the less viscous nature of both AM-dECM and E-dECM, both inks exhibited a shear-thinning behavior compatible with extrusion printing (Figure 3A′,A″).

Prior to bioprinting the ECM-derived bioinks with cells, it was imperative to demonstrate their biocompatibility. Therefore, we performed Live/Dead staining of human dermal fibroblasts (HDFs) cultured with D-dECM (Figure 3B) and a co-culture of 451Lu and WM164 melanoma cells cultured with AM-dECM and

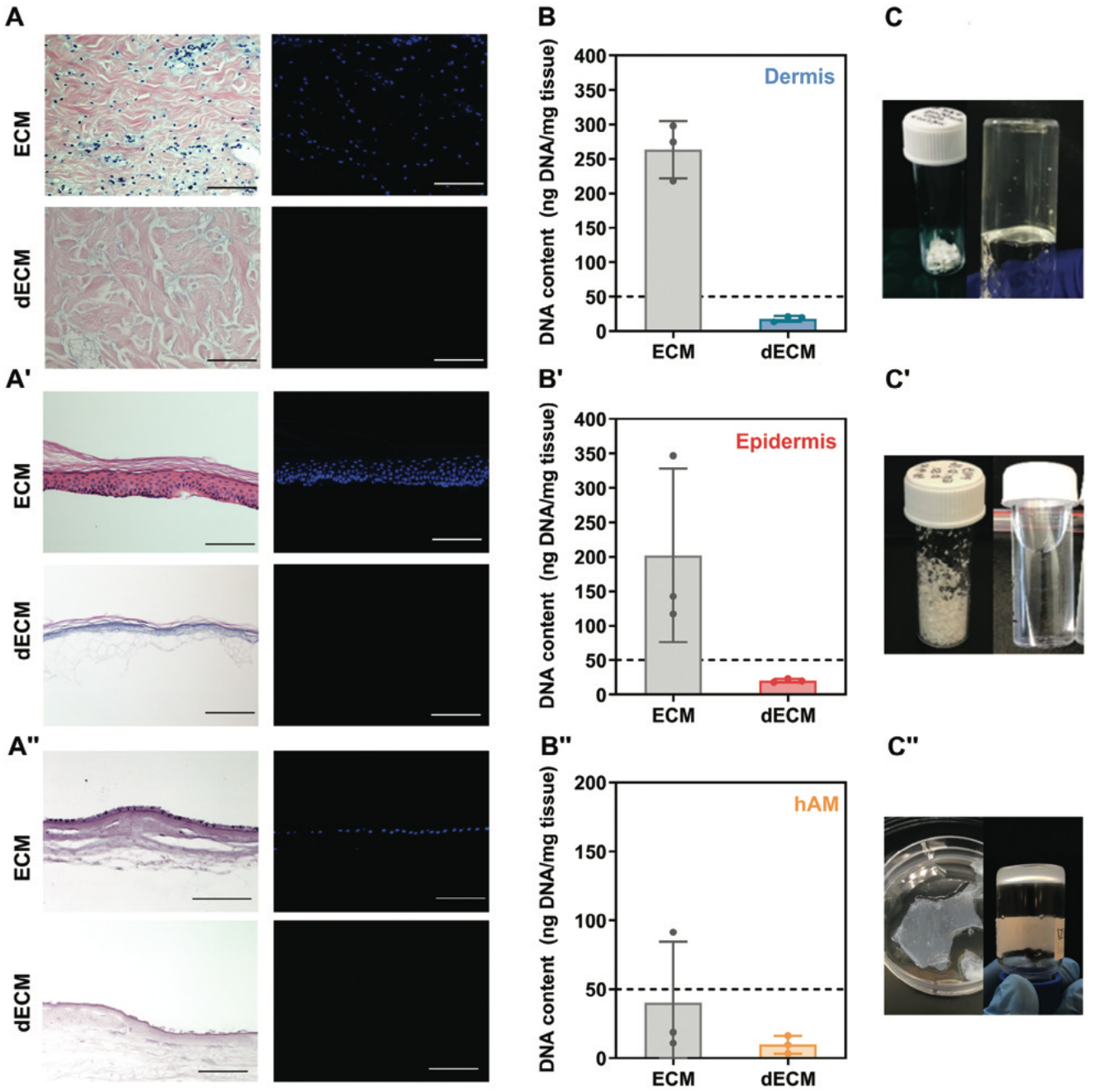

Figure 2. Characterization of tissue and dECM derived from porcine dermis A–C) and epidermis A′–C′), and human amniotic membrane A″–C″). A, A′, A″) Histological analysis of ECMs/dECMs, comprising hematoxylin and eosin staining (left) and DAPI fluorescence (right). Scale bars: 100 µm. B, B′,B″) DNA content of native and decellularized ECMs, with an acceptance criterion of <50 ng mg^{-1}. (C, C′, C″) Macroscopic images of dECMs (left) and inks (right).

E-dECM (Figure 3B′,B″). In all cases, excellent biocompatibility of the bioinks was demonstrated with the Hs27 human fibroblast cell line and corroborated by two alternative assays: CCK-8 assay for metabolic activity, and DNA release quantification by CellTox Green (Figure 3C). Interestingly, cells cultured with AM-dECM exhibited higher viability and metabolic activity values than the control, suggesting that this bioink may enhance cell growth. Finally, scanning electron microscopy (SEM) of a cross-section of lyophilized D-dECM revealed a highly heterogeneous material, composed of randomly oriented structures and cavities where cells might adhere and grow (Figure 3D). Overall, fully printable and biocompatible bioinks were developed to mimic the dermal, basement membrane, and epidermal compartments of the skin.

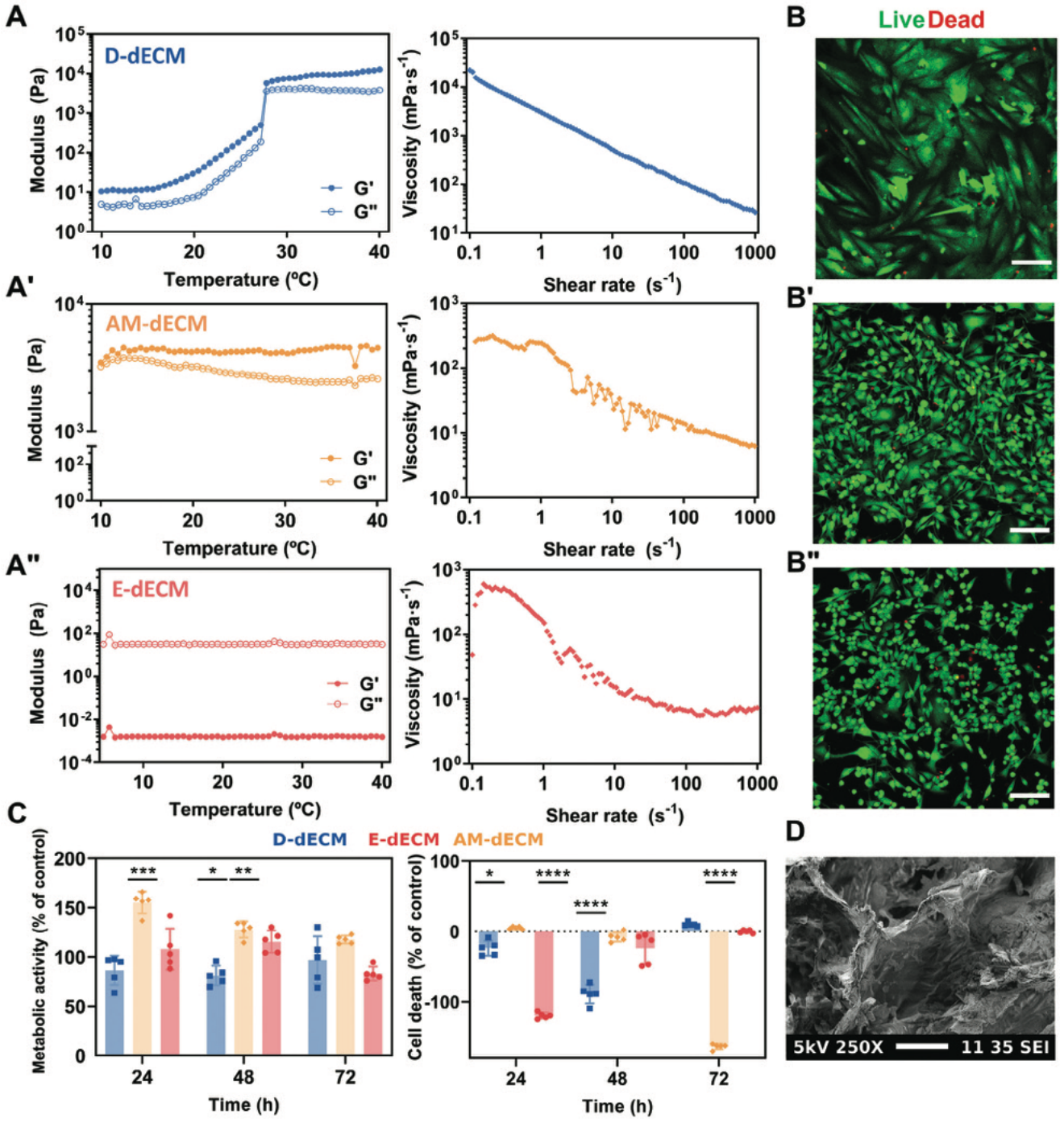

Figure 3. Characterization of dECM bioinks derived from dermis (D-dECM; blue), amniotic membrane (AM-dECM; orange), and epidermis (E-dECM; red). A,A′,A″) Rheological characterization by temperature ramp tests (left) and viscosity curves (right). B,B′,B″) Live/Dead staining of HDFs cultured with D-dECM B), 451Lu and WM164 melanoma cells cultured with AM-dECM B′), and E-dECM (green: calcein-AM; red: propidium iodide) B″). Scale bars: 150 µm. C) Cellular metabolic activity (left) and death ratio (right) of Hs27 cells incubated with dECM inks and normalized against positive and negative controls. D) Scanning electron microscopy image of the cross section of the acellular dermis dECM gel. Scale bar: 100 µm.

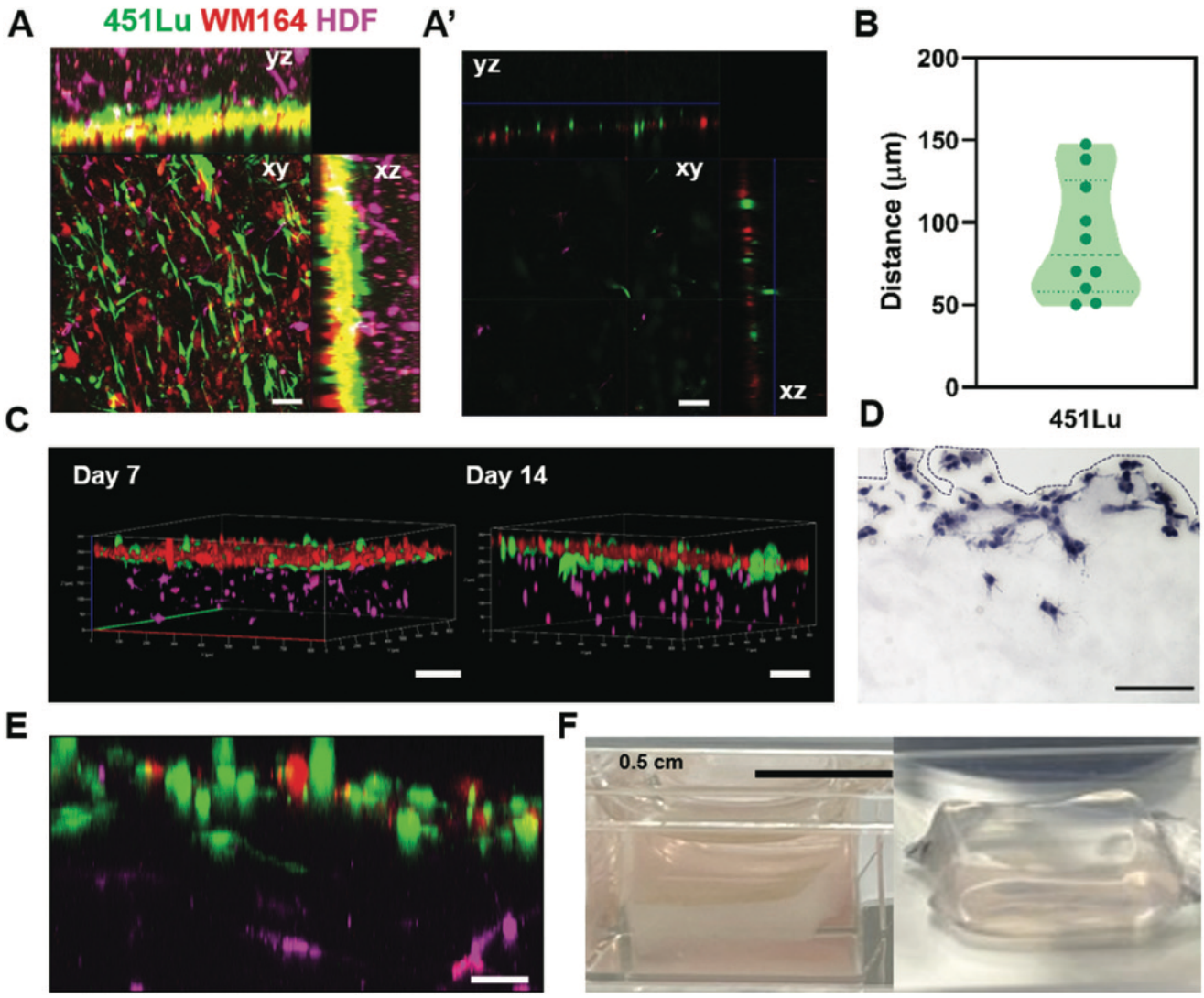

Figure 4. 3D printed layered melanoma model to simulate cancer cell invasion. A) Orthogonal view of maximum intensity projection of melanoma cells in the epidermal layer (green: 451Lu; red: WM164) on top of the HDF-loaded dermis (magenta), after 14 days in culture. Scale bar: 100 µm. A') Single plane detail of a protrusion of a 451Lu metastatic cell (green) deeper in the dermis gel. Scale bar: 100 µm. B) Quantification of the invasion distance by 451Lu cells. C) 3D reconstruction of the 3D printed model after 7 days (left) and 14 days (right) in culture. Scale bars: 150 µm. D) Hematoxylin/Eosin staining of the melanoma cells invading the dermal dECM. Scale bar: 100 µm. E) Transversal view of the microtissue with 451Lu cells migrating toward HDF-loaded D-dECM. Scale bar: 50 µm. F) Macroscopic view of the 3D printed layered melanoma model after 14 (left) and 21 days in culture (right).

2.2. Multimodal Imaging of Invasive Cells Within the 3D Melanoma Model

The three dedicated bioinks were successively printed to form a layered structure, and each cell type was labeled with fluorescent dyes and SERS tags, for confocal and SERS imaging, respectively. Since we were interested in mimicking and monitoring tumor cell invasion or metastasis into other tissues, the lower layer consisted of a healthy dermal compartment composed of HDF-loaded D-dECM, whereas the upper layer was a co-culture of both melanoma cell lines in the E-dECM, representing the tumor. For the generation of this layer, 451Lu cells were transfected to express green fluorescent protein (eGFP), whereas WM164 cells were transfected to express red fluorescent protein (RFP). In between those two layers, we printed a cell-free layer made of AM-dECM ink, to foster cell adhesion and thereby emulate the human basement membrane (Figure S5, Supporting Information). Crossing of the BM layer by 451Lu cells may thus be interpreted as penetration of melanoma cells from the epidermal to the dermal layer, as in the initial stages of melanoma dissemination.

As hypothesized, 451Lu cells were observed to migrate vertically through the layered model (**Figure** 4A,A'), demonstrating its validity to recreate the initiation of a metastatic process toward the healthy dermis, in radial growth phase melanoma. 451Lu cells were observed to migrate down 150 µm deep (average distance of 75 µm) (Figure 4B). Importantly, and as would be expected, this effect was not observed for WM164 cells. Although earlier time points were assessed (Figure S4A, Support-

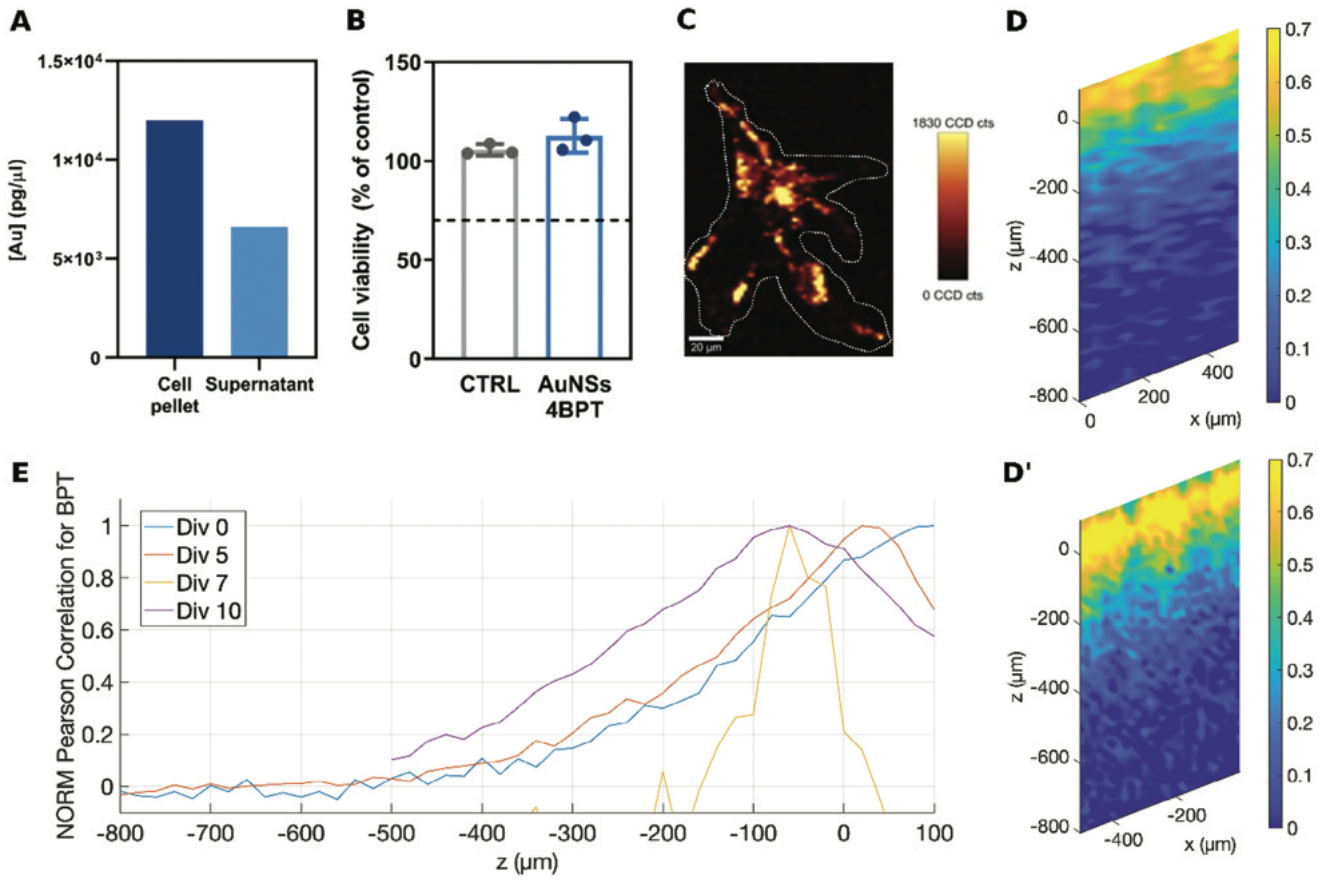

Figure 5. SERS monitoring of cancer cell invasion. A) ICP-MS quantification of the uptake of AuNSs by pooled 451Lu cells (pool of $n = 3$). B) Cell viability assessment (mean ± SD) after overnight incubation of 451Lu cells with 50×10^{-6} M AuNS@4BPT ($n = 3$). C) 2D SERS mapping of 4BPT SERS tags in 451Lu cells. Scale bar: 20 µm D) Distribution of 4BPT SERS signal along the Z axis by means of the Pearson's correlation coefficient, with reference AuNS@4BPT, after 0 days and D′) 5 days in culture. E) All spectra at the same Z-coordinate in each SERS mapping were averaged and analyzed by Pearson's correlation against AuNS@4BPT. A comparison is shown for the 4BPT signals along the Z axis after 0, 5, 7, and 10 days in culture. The distributions are normalized for clarity.

ing Information), at least 7 days were required for 451Lu migration to be detected (Figure S4B, Supporting Information). After 2 weeks, we observed 451Lu-GFP cells invading the lower HDF-containing D-dECM layer, and they were found in the vicinity of fibroblasts (Figure 4C). This observation was confirmed in Hematoxylin/Eosin sections (Figure 4D). Importantly, HDFs interacting with 451Lu cells exhibited their characteristic morphology (see Figure 4E and Figure S4C, Supporting Information). We also observed rapid growth of HDFs resulting in contraction of the microtissue (Figure S4D, Supporting Information). Interestingly, despite the activity of the cells within the dECM, hydrogels retained their properties and were not degraded after 21 days in culture, which is a common drawback when working with Matrigel or similar materials (Figure 4F).

When building 3D models to mimic biological processes, fluorescence is the main technique of choice for imaging and monitoring. However, fluorescence imaging presents limited imaging depth and multiplexing possibilities. In contrast, SERS imaging benefits from deeper penetration depth when using a NIR excitation laser, as well as high flexibility in the choice of RaRs for multiplex labelling and discrimination of different cell populations or structural layers. Indeed, AuNPs can be encoded with various RaRs, as previously reported,[33,37] and incorporated in the 3D printed system. Therefore, we labelled 451Lu-eGFP cells with 4-bisphenylthiol (4BPT)-encoded AuNSs (AuNS@4BPT) (Figure S5, Supporting Information), whereas WM164-RFP cells were labelled with 2-naphthalenetiol (2NAT)-encoded AuNSs (AuNS@2NAT). The cell-free layer of AM-dECM ink contained 4-methyl benzenethiol (4bpt)-labelled AuNSs (AuNS@4MBT). Full details on the synthesis and characterization of SERS tags are described in the Experimental section and in Figures S6–S8 (Supporting Information).

With the objective of monitoring metastasis initiation, we first measured NP uptake by 451Lu cells using inductively coupled plasma mass spectrometry (ICP-MS), and conducted cell viability studies of cells incubated in the presence of SERS tags overnight, similarly to previous studies.[33] AuNSs were taken up by 451Lu cells (**Figure** 5A) without compromising their viability (Figure 5B and Figure S6D, Supporting Information). Cellular uptake of the tags was confirmed by high-magnification SERS imaging of 451Lu cells labelled with AuNS@4BPT (Figure 5C).

Considering the biocompatible nature of both SERS tags and dECM inks, we used SERS to monitor the migration of cells over time. Mappings consisting of SERS spectra recordings of the

selected areas within the constructed 3D melanoma model were acquired in XZ planes. Each Raman spectrum was compared with a reference spectrum acquired from AuNS@4BPT, using Pearson's correlation coefficients (*R*) for evaluation. These may span from 0, or below for negative matching, to 1 in case of a perfect match with the reference.[56] Figure 5D,D′ reports the analyzed slices in false colors relative to the R values. The signal corresponding to 451Lu cells labelled with AuNS@4BPT was identified at lower Z depths as time progressed, suggestive of cell invasion (Figure 5D,D′). This effect was observed after 5 days in culture, suggesting that SERS can indeed be used to detect cell displacements at initial stages of cell migration. To better analyze the diffusion of the 4BPT SERS signal in Z over time, spectra at the same Z position were averaged and queried against their correspondence with the AuNS@4BPT reference, by Pearson's correlation (Figure 5E).[33] A shift of the maximum of the SERS signal distribution toward deeper layers was clearly registered after 5 days, and even more pronounced at 10 days (Figure 5E and Figure S9, Supporting Information). These results confirmed that the SERS imaging is fit to monitor cancer cell migration. It could also be used to monitor other biological events at early time points.

2.3. Anticancer Drug Testing

Use of in vitro 2D models and animal models has resulted historically in high drug attrition rates, due to the different response of these models as compared to patients. In melanoma patients, the overexpression of vascular endothelial growth factor A (VEGF-A) is known to promote melanoma growth and metastasis, and it correlates with poor overall survival.[57] PLX4032, also known as Vemurafenib, is an FDA-approved drug that inhibits B-Raf kinase by selectively binding to its ATP-binding site.[6] BRAF V600 mutations are present in more than 40% of melanoma patients, resulting in the aberrant activation of MAPK signaling pathway. PLX4720, a sister compound of Vemurafenib, has potent antimigratory and anti-invasive properties. It inhibits B-Raf V600, and is commonly used in preclinical studies.[58] Therefore, as a proof of concept of anticancer drug testing, we exposed the 3D printed microtissues to different concentrations of VEGF-A, PLX4720, and PLX4032, and the results were consistent with literature data,[6,58,59] as confirmed by both CellTox Green assay and CLSM imaging (**Figure 6**A,B).

VEGF-A induced a significant increase in cell proliferation after 48 hours and reduced cell death as compared to untreated controls (Figure S10A, Supporting Information). This effect remained evident after 7 days of exposure, which was reflected in an increased cell density, as well as an increase in the mean gray value (brightness level of a pixel) (Figure 6C,D). In contrast, PLX4720 displayed considerable cytotoxicity, particularly toward melanoma cells at shorter time points, which was intensified over time. Similar results were observed for PLX4032, which was cytotoxic to most melanoma cells. Exceptionally, a few 451Lu cells survived the treatment and those that remained viable showed continued growth after 14 days in vitro, possibly due to acquired resistance (Figure S10B, Supporting Information).[59–61] Both PLX4032 and PLX4720 had none or little effect on the integrity of HDFs (Figures S10C,D and S11, Supporting Information). Complementary results related to drug testing assays are presented in Figures S12 and S13 (Supporting Information).

The effect of VEGF-A in promoting cell proliferation was also followed by SERS. Analysis of the 3D reconstructions of treated models confirmed the identification of all three signals, corresponding to 4BPT, 2NAT, and 4MBT (Figure 6E). These results demonstrated that distinct labelling of metastatic and non-metastatic cells within the BM-like layer may be achieved. In fact, the signal became more widespread over time and was visible after 21 days (Figure S14, Supporting Information). Extended cell culture time points may pose a challenge when employing live cell fluorescence dyes, such as CellTracker, because this technique is typically effective for only 3 to 6 generations due to tracker dilution at every cell cycle. In contrast, a lower overall signal was recorded for 2NAT whereas 4MBT was clearly detectable and partially overlapped with the 4BPT signal. These observations may be attributed to the 451Lu cells having internalized AuNS@4MBT that were freely dispersed in the AM-dECM solution. The mappings obtained on day 7 showed a reduced overall intensity, which is likely a result of the previously discussed factors.

3. Conclusions

This study addressed cell heterogeneity, layered materials, pharmacological resistance, and how the 3D nature of the proposed melanoma model affects the impact of selected drugs. Nonetheless, several limitations persist, which could be addressed, e.g., by improving the printability of the material, replacing cell lines with patient-derived cells, and testing different therapies and conditions on the model, such as hypoxia or immunotherapeutic agents. Additionally, future studies should aim to incorporate vascular and immune cells into more complex systems.

In summary, we have described the use of dECMs as printable bioinks, suitable for the construction of a 3D in vitro melanoma model. Previous 3D printed models do not examine the biological relevance of the materials.[17,55,62] In this regard, traditional basement membrane extracts are not suitable for BM modelling because they are often tumor-derived ECMs. Furthermore, dhAM has been acknowledged as an excellent BM model, and in this study we have integrated this material of vital biological significance into a realistic 3D system. Although 3D SERS bioimaging is still at an early stage of development and requires complex data analysis, by combining fluorescence imaging and SERS we achieved simultaneous and multimodal imaging of living complex models and biological processes, demonstrating the presence of metastatic cells capable of invading the healthy tissue (dermis). The biofabrication of layered cancer models could be adapted to imitate the architecture of different solid tumors, and their coupling with CLSM and SERS may enlighten mechanisms behind the complexity of cancer behavior at early stages. Finally, we verified the suitability of the 3D microtissue for long-term cell culture and as a drug screening system. The fabrication of multiple replicates of the developed model at the required scale would permit to test different compounds and dosages simultaneously and thus enable translation of the basic findings presented here to the pharmaceutical industry.

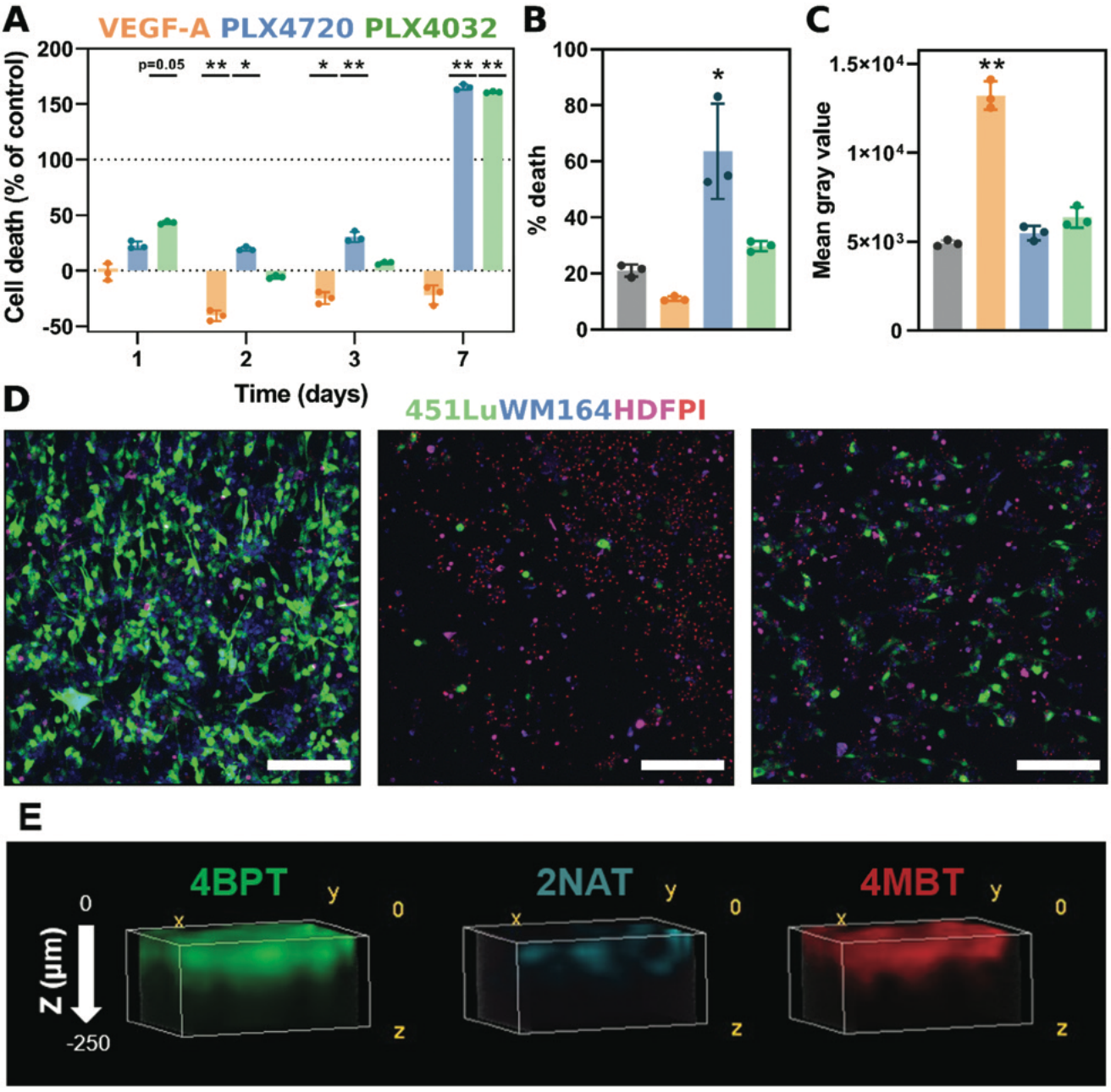

Figure 6. 3D layered melanoma model as a drug testing platform. A) CellTox Green assay results after exposing a 3D microtissue to 100 ng mL^{-1} VEGF-A (protumoral; orange), PLX4720 (antitumoral; blue), and PLX4032 (antitumoral; green). Data ($n = 3$) normalized against positive and negative controls is presented as mean ± SD. * = $P < 0.05$ and ** = $P < 0.01$. B) Quantification of CLSM imaging of cell death and C) mean gray value of the models after 7 days of exposure to the drug (mean ± SD of $n = 3$). D) Maximum intensity projections of a 3D melanoma model after 7 days of exposure to 100 ng mL^{-1} VEGF-A (left), 20×10^{-6} M PLX4720 (center), and 75×10^{-9} M PLX4032 (right). Green: 451Lu; Blue: WM164; Magenta: HDF; Red: PI. Scale bars: 200 µm. E) 3D reconstructions of SERS mappings for VEGF-A treated samples for 7 days. 451Lu cells labelled with 4BPT, WM164 with 2NAT and BM with 4MBT.

4. Experimental Section

Instrumentation: Histological sections were made either with a HM 355S microtome (Thermo Fisher Scientific) or a CM1950 cryostat (Leica). dECM was ground with a PuLVRisette 14 mill (Fritsch). Plate readers Glo-Max Discover (Promega) and Appliskan (Thermo Fisher Scientific) were used in this work. Rheological properties were measured using a MCR302 rheometer (Anton Paar), equipped with a 25 mm cone and plate geometry, with a water solvent trap to avoid sample evaporation and ensure a saturated atmosphere. Scanning electron microscopy (SEM) images were acquired with a JSM-6490LV (JEOL) operating at an acceleration voltage of 5 kV. Transmission Electron Microscopy (TEM) was done with a JEM-

1400PLUS (JEOL) operating at an acceleration voltage of 120 kV. 3D printing was conducted with a 3DDiscovery printer (RegenHU). Confocal laser scanning microscopy imaging was performed with a LSM880 microscope (Zeiss), equipped with Ar, DPSS and HeNe lasers, and Plan-Apochromat 10× (0.45 NA) and Plan-Apochromat 20× (0.8 NA) objectives. Raman microscopes InVia Reflex (Renishaw) and alpha300 R (WITec) were used to record the different SERS spectra and maps. UV-Vis spectroscopy was carried out using a 8453 diode-array spectrophotometer (Agilent).

Materials: Ethanol, peracetic acid, glacial acetic acid, SDS solution, Tris-EDTA buffer solution, EDTA, NaOH, NH_4Cl, Triton X-100, DPX mountant, proteinase K, deoxyribonucleic acid from calf thymus, tumor specialized medium (TSM; MCDB 153 medium, sodium bicarbonate solution, $CaCl_2$, L-15 medium), 0.5% trypsin/EDTA solution 10X, penicillin-streptomycin, Cell Counting Kit-8 (CCK-8) and VEGF-A were all purchased from Sigma-Aldrich. Histofix, Harris Hematoxylin and Eosin Yellowish alcoholic solution 1% were purchased from PanReac AppliChem. CellTox Green was acquired from Promega. Quant-iT PicoGreen dsDNA assay kit, CellTracker, DMEM, fetal bovine serum, Fluoromount-G mounting medium, DAPI and Live/Dead Viability/Cytotoxicity Kit, were purchased from ThermoFisher. Denarase was purchased from c-Lecta. PLX4720 and PLX4032 were purchased from MedChemExpress.

451Lu and WM164 cell lines were purchased from Rockland and HDFs from Invitrogen (Thermo Fisher Scientific).

Milli-Q water (resistivity 18.2 MΩ cm) was used in all AuNP synthesis experiments. Hydrogen tetrachloroaurate trihydrate ($HAuCl_4 \cdot 3H_2O$, ≥99.9%), sodium citrate tribasic dihydrate (≥98%), silver nitrate, ($AgNO_3$, ≥99%), L-ascorbic acid (AA, ≥99%), O-[2-(3-mercaptopropionylamino)ethyl]-O′-methylpolyethylene glycol (PEG, MW 5000 g mol^{-1}), 2-naphthalenethiol (2-NAT, 99%), 4-methylbenzenethiol (4-MBT, 98%), biphenyl-4-thiol (4-BPT, 97%), 4-poly(isobutylene-alt-maleic anhydride), (PMA, average Mw ~ 6000 g mol^{-1}), dodecylamine (98%), chloroform ($CHCl_3$, ≥99.8%) and poly-L-arginine hydrochloride (PA) were also purchased from Sigma-Aldrich.

dECM Ink Preparation: Porcine dorsal skin tissue was obtained from the slaughterhouse and 0.5 mm sheets were obtained with a D80 dermatome (Humeca) and stored at −80 °C. The tissue was thawed in a water bath at 56 °C for 30 min to physically separate the dermis and the epidermis. The dermis was decellularized according to Wolf et al. with slight modifications.[52] Briefly, a 40 U mL^{-1} denarase treatment overnight at 37 °C under constant agitation was included prior to the peracetic acid/ethanol step. The epidermis was treated with 0.5% (w/v) SDS solution for 2 hours at RT under constant agitation and washed thrice with distilled water. Human amniotic membranes (hAMs) were collected upon approval by the human research ethics committee of the Hospital Universitario Donostia (CEI Area Gipuzkoa; AIP-HAM-2021-01) and stored at −80 °C until needed. The hAMs were exposed to 0.2% (w/v) EDTA for 30 minutes at 37 °C and washed with 0.5 M NaOH and 5% (w/v) NH_4Cl for 30 s each at RT and later rinsed thrice in PBS, following the protocol detailed by Mazaher et al.[63] Every tissue was sterilized with 0.1% (v/v) peracetic acid and 4% (v/v) ethanol for 2 hours and later washed twice with PBS and twice with distilled water. The final step of freeze-drying for 72 hours was performed for every dECM prior to grinding. dECMs were ground with a PuLVRisette 14 mill (Fritsch). The dermal ink (D-dECM) was obtained by digesting 5 mg of dECM powder per mL of 1 mg mL^{-1} pepsin in 0.5 M acetic acid solution for 72 h. The epidermal ink (E-dECM) was produced by digesting 10 mg of epidermis powder per mL of 10 M NaOH for 48 hours. For the hAM ink (AM-dECM), 25 mg of dECM was digested in a 2 mg mL^{-1} pepsin solution in 0.01 N HCl for 48 hours. The pH of every solution was adjusted to pH 7.4 on ice. D-dECM and AM-dECM were used directly while E-dECM was dialyzed against distilled water for 72 hours, freeze-dried again and later dissolved in tumor specialized media (TSM) to a final concentration of 1 mg mL^{-1}. A summary table of the protocols is available in Table S1 (Supporting Information).

Histology of the ECM and dECM: The tissues were fixed in Histofix overnight at 4 °C and embedded in paraffin. Histological sections were made with a HM 355S microtome (Thermo Fisher Scientific). 5 µm tissue sections stained with 1 µg mL^{-1} DAPI for 30 minutes after re-hydration and permeabilizing the tissue with 0.3% (v/v) Triton X-100 for 30 min and mounted in Fluoromount-G. Hematoxylin/Eosin staining protocols were optimized for each tissue and mounted in DPX mountant.

DNA Quantification: 5 mg of each tissue were digested in 500 µL of digestion buffer (100×10^{-3} M Tris, 2×10^{-3} M EDTA, 150×10^{-3} M NaCl, 1% (w/v) SDS and 200 µg mL^{-1} of proteinase K) for 48 hours at 56 °C. DNA was manually precipitated with ethanol as described by Green et al.[64] The amount of DNA in the native and the decellularized tissues was quantified with the Quant-iT PicoGreen dsDNA assay kit. Standards were prepared using calf thymus DNA in 1X Tris-EDTA buffer. Samples in 96-well plates were excited at 492 nm and emission was recorded at 535 nm in an Appliskan microplate reader.

Material Characterization: Measurements for assessing rheological properties of cell-free hydrogels were performed on a MCR302 rheometer (Anton Paar) equipped with a 25 mm diameter cone-plate geometry, a Peltier plate at 10 °C for noncrosslinked samples and 37 °C for the crosslinked ones, and a humidity chamber to maintain the samples hydrated during the measurements. Amplitude sweeps, frequency sweeps, viscosity ramps and temperature ramps measurements were performed with 50 µm gap size. The excess material was trimmed prior to starting the measurements.

Swelling behavior was evaluated by printing three replicates per timepoint. Hydrogels were crosslinked for 30 minutes at 37 °C and weighed after freeze-drying. Samples were incubated in TSM supplemented with 2% FBS for 15′, 30′, 1 h, 2 h, 72 h, and 7 days, and weighed at different timepoints.

The biocompatibility study was performed by incubating cells directly with crosslinked 2 mm diameter D-dECM and AM-dECM disks or 1/10 volumes E-dECM in 96-well plates. CCK-8 kit and CellTox Green kits were used following the corresponding manufacturer's protocols for cytotoxicity evaluation. Plates were read with Appliskan (Thermo Fisher Scientific) and GloMax Discover (Promega) respectively. For Live/Dead Viability/Cytotoxicity assay, cells were incubated on top of 8 mm disks or with 1/10 volumes E-dECM in a 24-well plate.

For SEM imaging, cell-free hydrogels were cross-linked for 30 minutes at 37 °C, freeze-dried and coated with a thin gold/palladium layer by magnetron sputtering, before being imaged with a JSM-6490LV microscope (JEOL) with a working distance of 10 mm and 5 kV voltage.

AuNS and SERS Tag Synthesis: AuNSs were prepared following a reported seed-mediated growth method.[65] The synthetized AuNSs with LSPR maximum at 800 nm were then coated with O-[2-(3-mercaptopropionylamino)ethyl]-O′-methylpolyethylene glycol (PEG-SH, MW 5000 g mol^{-1}) and labeled with Raman reporters, following a previously described protocol.[37] 2NAT, 4BPT and 4MBT molecules were used for such purpose and, due to their hydrophobic nature, the resulting AuNSs were coated with the amphiphilic polymer PMA, to make them hydrophilic and biocompatible, and further covered with poly-L-arginine hydrochloride (PA) to impart an overall positive surface charge, known to enhance cell uptake.

Cell Culture and Fluorescence Imaging: Melanoma cell lines 451Lu and WM164 were cultured in TSM supplemented with 2% FBS. HDFs and Hs27 were cultured in DMEM supplemented with 10% FBS. Every cell line was fluorescently labelled independently with live cell tracking fluorophores (CellTracker) or transfected to express GFP (pLenti CMV GFP Hygro (656-4, Addgene) or RFP (pLenti CMV RFP Hygro (LVP1226, AMSBIO), according to the manufacturer's instructions. The metabolic activity of live cells was determined by CCK-8 kit while cell death was assessed through CellTox Green and Live/Dead Viability/Cytotoxicity Kit following the corresponding manufacturer's protocols for cytotoxicity evaluation.

3D Printing: The 3D melanoma model was printed with a 3DDiscovery Evolution printer (regenHU) equipped with a biosafety cabinet. 24 hours prior to printing, 451Lu and WM164 cells were incubated with 25×10^{-6} M AuNS@4BPT and 25×10^{-6} M AuNS@2NAT respectively overnight at 37 °C. HDFs were mixed with D-dECM in complete DMEM (final cell concentration 5×10^5 HDFs mL^{-1}), and 2×10^6 451Lu cells and 2×10^6 WM164 cells were mixed per mL of 1 mg mL^{-1} E-dECM in TSM. Cell-loaded D-dECM was printed into 8-well chambers (Ibidi) using a 27G needle and feed rate of 1 mm s^{-1} and 0.035 MPa pressure, followed by incubation for 30 min at 37 °C. Two layers of AM-dECM loaded with 50×10^{-6}

M AuNS@4MBT were printed on top of the D-dECM using a cell-friendly cartridge connected to a compressed air system delivering a pressure of 0.025 MPa and to the microvalve actuator with a feed rate of 15 mm s^{-1} and opening and closing time of 500 and 300 ms respectively. After 1 hour incubation at 37 °C, 7 layers of melanoma cell-loaded E-dECM suspension were printed in the same manner, constituting the top layer of the 3D microtissue. The printing patterns were drawn via BioCAD software (regenHU).

Imaging: For SERS measurements, the samples were placed on a quartz slide (24×60 mm) and a custom-made 3D printed holder (to immerse the SERS objective) was placed on top and glued using two component silicon dentist-gel (Proclininc Products). Cell medium or PBS was then added to avoid scaffold drying. SERS spectra were obtained using a InVia Reflex confocal Raman microscope (Renishaw) comprising of an optical microscope (Leica) with an XYZ scanning stage (Prior) and equipped with a Peltier-cooled front-illuminated 1024×512 CCD detector and a 1200 L mm^{-1} diffraction grating. For the experiments a 785 nm laser excitation source and a 40× water immersion objective (numerical aperture, NA = 0.8) were used. An integration time of 1 seconds at 36 mW laser power at surface (50% of the maximum power) was employed while recording the Raman signal in static mode at standard confocality mode through the same objective. Maps of the selected area of the model were acquired with a resolution of 50 or 20 µm in X and Z. SERS data were first analyzed using the WiRE4.4 software (Renishaw, Wotton-under Edge, U.K.) to correct the baseline in the spectra and eliminate cosmic rays. SERS mappings were analyzed by Pearson's correlation in MATLAB, with the reference spectra of each tag which considers the full spectrum to assign the typical fingerprints of each SERS tag. High-resolution SERS mapping was obtained by using a confocal Raman microscope (WITec, GmbH, Germany) containing of a microscope (Zeiss) fiber-coupled to a high-throughput spectrometer equipped with a 300 g mm^{-1} grating and a Peltier-cooled back-illuminated deep-depletion CCD camera. The experiments were carried out through an N-Achroplan 20× water immersion objective (NA = 0.5) using a laser power of 5 mW (True power) and an integration time of 50 ms. The Project FIVE software (WITec, GmbH, Germany) was applied to remove cosmic rays, subtract the baseline (method: shape), analyze the fingerprint (True Components) and plot the SERS intensity of the detected 4-BPT components as a function of the position.

Drug Testing: VEGF-A stock (100 µg mL^{-1} in dH_2O) was diluted in TSM to a final concentration of 100 ng mL^{-1}. PLX4032 stock (10×10^{-3} M in DMSO) was diluted in TSM to a final concentration of 75×10^{-9} M. PLX4072 stock (10×10^{-3} M in DMSO) was diluted in TSM to a final concentration of 20×10^{-6} M. Melanoma models were sequentially printed into 48-well plates and after 1 day they were exposed to either VEGF-A, PLX4032, PLX4072 or TSM for 21 days. Cell media was collected, and drug cytotoxicity was measured using the CellTox Green assay according to manufacturer instructions. Drug-containing medium was refreshed every 2–3 days. Prior to CLSM imaging, 3×10^{-6} M propidium iodide was added to every well. Data shown in graphs are the summary of three biological replicates in three independent experiments, normalized to negative (control) and positive (Triton-X) cell death controls.

Statistical Analysis: Bar graphs and point graphs display mean value ± SD. The normality of data distribution was determined using the Kolmogorov–Smirnov test. Unpaired Student's *t*-tests were conducted for single mean comparisons or one-way ANOVA for multiple mean comparisons when data followed a normal distribution. Two-way ANOVA was used for differences in the effects of independent variables on a dependent variable. Data not following a normal distribution were analyzed using the nonparametric Bonferroni's test for multiple mean comparisons. Significance threshold was set at $P < 0.05$. Significance levels were assigned as follows: * = $P < 0.05$, ** = $P < 0.01$, *** = $P < 0.001$, **** = $P < 0.0001$. Statistical analyses and graphs were performed using GraphPad Prism 8.3.0 software (GraphPad, San Diego, CA).

Schemes and Cartoons: Figures, schemes and cartoons were created with Inkscape.

Ethics Approval Statement: Human amniotic membranes (hAMs) were collected upon approval by the human research ethics committee of the Hospital Universitario Donostia (CEI Area Gipuzkoa; AIP-HAM-2021-01)

Patient Consent Statement: Informed consent was obtained from all donors included in the study (AIP-HAM-2021-01).

Supporting Information

Supporting Information is available from the Wiley Online Library or from the author.

Acknowledgements

P.V.-A. was supported by a fellowship paid by the donation made by Asociación Katxalin in 2019. C.G.A. thanks MINECO for the Juan de la Cierva Incorporación Fellowship IJC2019-040827-I. P.V.-A. and A.I. thank F.J. Nicolás for providing the first hAM sample. The authors acknowledge financial support from the European Research Council (ERC-AdG-2017#787510), the Instituto de Salud Carlos III (PI22/01247 and PT23/00142), co-funded by the European Union; Diputación Foral de Gipuzkoa; and the Department of Health (2020111004; 20BU206) and the Department of Economy and Competitiveness of the Basque Government (KK-2020/00010; KK-2019/00006; KK-2019/00093). This work was performed under the Maria de Maeztu Units of Excellence Program from the Spanish State Research Agency, grant no. MDM-2017-0720.

Conflict of Interest

The authors declare no conflict of interest.

Data Availability Statement

The data that support the findings of this study are available from the corresponding authors upon reasonable request.

Keywords

3D bioprinting, dECM, melanoma, metastasis, SERS

Received: March 26, 2024
Revised: June 27, 2024
Published online:

[1] G. Kyriakou, M. Melachrinou, *Future Oncol.* **2020**, *16*, 1549.
[2] D. Hanahan, *Cancer Discov.* **2022**, *12*, 31.
[3] P. Karras, I. Bordeu, J. Pozniak, A. Nowosad, C. Pazzi, N. Van Raemdonck, E. Landeloos, Y. Van Herck, D. Pedri, G. Bervoets, S. Makhzami, J. H. Khoo, B. Pavie, J. Lamote, O. Marin-Bejar, M. Dewaele, H. Liang, X. Zhang, Y. Hua, J. Wouters, R. Browaeys, G. Bergers, Y. Saeys, F. Bosisio, J. Van Den Oord, D. Lambrechts, A. K. Rustgi, O. Bechter, C. Blanpain, B. D. Simons, et al., *Nature* **2022**, *610*, 190.
[4] S. Fernandes, C. Vyas, P. Lim, R. F. Pereira, A. Virós, P. Bártolo, *3D Bioprinting: Cancers* **2022**, *14*, 3535.
[5] A. Marconi, M. Quadri, A. Saltari, C. Pincelli, *Exp. Dermatol.* **2018**, *27*, 578.
[6] D. Morales, F. Lombart, A. Truchot, P. Maire, M. Hussein, W. Hamitou, P. Vigneron, A. Galmiche, C. Lok, M. Vayssade, *Tissue Eng. Part A* **2019**, *25*, 1116.

[7] C. Jubelin, J. Muñoz-Garcia, L. Griscom, D. Cochonneau, E. Ollivier, M.-F. Heymann, F. M. Vallette, L. Oliver, D. Heymann, *Cell Biosci.* **2022**, *12*, 155.
[8] M. A. G. Barbosa, C. P. R. Xavier, R. F. Pereira, V. Petrikaitė, M. H. Vasconcelos, *Cancers* **2021**, *14*, 190.
[9] A. Filipiak-Duliban, K. Brodaczewska, A. Majewska, C. Kieda, *In Vitro Cell Dev. Biol.-Animal* **2022**, *58*, 349.
[10] P. Zamora-Perez, C. Xiao, M. Sanles-Sobrido, M. Rovira-Esteva, J. J. Conesa, V. Mulens-Arias, D. Jaque, P. Rivera-Gil, *Acta Biomater.* **2022**, *142*, 308.
[11] R. Schmid, S. K. Schmidt, R. Detsch, H. Horder, T. Blunk, S. Schrüfer, D. W. Schubert, L. Fischer, I. Thievessen, S. Heltmann-Meyer, D. Steiner, D. Schneidereit, O. Friedrich, A. Grüneboom, H. Amouei, H. Wajant, R. E. Horch, A. K. Bosserhoff, A. Arkudas, A. Kengelbach-Weigand, *Adv. Funct. Mater.* **2022**, *32*, 2107993.
[12] I. Müller, D. Kulms, *JoVE* **2018**,*135*, 57500.
[13] A. Olejnik, J. A. Semba, A. Kulpa, A. Dańczak-Pazdrowska, J. D. Rybka, J. Gornowicz-Porowska, *ACS Synth. Biol.* **2022**, *11*, 26.
[14] B. Bhar, E. Das, K. Manikumar, B. B. Mandal, *Adv. Healthcare Mater.* **2024**,*13*, 2303312.
[15] D. Min, W. Lee, I. Bae, T. R. Lee, P. Croce, S. Yoo, *Exp. Dermatol.* **2018**, *27*, 453.
[16] Z. Pazhouhnia, A. Noori, A. Farzin, K. Khoshmaram, M. Hoseinpour, J. Ai, M. Ebrahimi, N. Lotfibakhshaiesh, *Sci. Rep.* **2024**, *14*, 12670.
[17] L. Pontiggia, I. A. Van Hengel, A. Klar, D. Rütsche, M. Nanni, A. Scheidegger, S. Figi, E. Reichmann, U. Moehrlen, T. Biedermann, *J. Tissue Eng.* **2022**, *13*, 204173142210885.
[18] M. Rafaeva, E. R. Horton, A. R. D. Jensen, C. D. Madsen, R. Reuten, O. Willacy, C. B. Brøchner, T. H. Jensen, K. W. Zornhagen, M. Crespo, D. S. Grønseth, S. R. Nielsen, M. Idorn, P. T. Straten, K. Rohrberg, I. Spanggaard, M. Højgaard, U. Lassen, J. T. Erler, A. E. Mayorca-Guiliani, *Adv. Healthcare Mater.* **2022**, *11*, 2100684.
[19] K. Bera, A. Kiepas, I. Godet, Y. Li, P. Mehta, B. Ifemembi, C. D. Paul, A. Sen, S. A. Serra, K. Stoletov, J. Tao, G. Shatkin, S. J. Lee, Y. Zhang, A. Boen, P. Mistriotis, D. M. Gilkes, J. D. Lewis, C.-M. Fan, A. P. Feinberg, M. A. Valverde, S. X. Sun, K. Konstantopoulos, *Nature* **2022**, *611*, 365.
[20] S. Kim, S. Min, Y. S. Choi, S.-H. Jo, J. H. Jung, K. Han, J. Kim, S. An, Y. W. Ji, Y.-G. Kim, S.-W. Cho, *Nat. Commun.* **2022**, *13*, 1692.
[21] E. A. Aisenbrey, W. L. Murphy, *Nat. Rev. Mater.* **2020**, *5*, 539.
[22] G. Benton, I. Arnaoutova, J. George, H. K. Kleinman, J. Koblinski, *Adv. Drug Delivery Rev.* **2014**, *79*, 3.
[23] A. Naba, K. R. Clauser, H. Ding, C. A. Whittaker, S. A. Carr, R. O. Hynes, *Matrix Biol.* **2016**, *49*, 10.
[24] B. S. Kim, S. Das, J. Jang, D.-W. Cho, *Chem. Rev.* **2020**, *120*, 10608.
[25] H. Kim, B. Kang, X. Cui, S.-H. Lee, K. Lee, D.-W. Cho, W. Hwang, T. B. F. Woodfield, K. S. Lim, J. Jang, *Adv. Funct. Mater.* **2021**, *31*, 2011252.
[26] S. Krishtul, L. Baruch, M. Machluf, *Adv. Funct. Mater.* **2020**, *30*, 1900386.
[27] Y. Kang, P. Datta, S. Shanmughapriya, I. T. Ozbolat, *ACS Appl. Biol. Mater.* **2020**, *3*, 5552.
[28] P. Vázquez-Aristizabal, G. Perumal, C. García-Astrain, L. M. Liz-Marzán, A. Izeta, *ACS Omega* **2022**, *7*, 16236.
[29] T. Weng, W. Zhang, Y. Xia, P. Wu, M. Yang, R. Jin, S. Xia, J. Wang, C. You, C. Han, X. Wang, *J Tissue Eng* **2021**, *12*, 204173142110285.
[30] A. Bhusal, E. Dogan, D. Nieto, S. A. Mousavi Shaegh, B. Cecen, A. K. Miri, *ACS Appl. Biol. Mater.* **2022**, *5*, 4480.
[31] J. Jonkman, C. M. Brown, G. D. Wright, K. I. Anderson, A. J. North, *Nat. Protoc.* **2020**, *15*, 1585.
[32] M. J. Sanderson, I. Smith, I. Parker, M. D. Bootman, F. Microscopy, *Cold Spring Harb Protoc* **2014**, *2014*, pdbtop071795.
[33] D. Jimenez De Aberasturi, M. Henriksen-Lacey, L. Litti, J. Langer, L. M. Liz-Marzán, *Adv. Funct. Mater.* **2020**, *30*, 1909655.
[34] K. Kneipp, Y. Wang, H. Kneipp, L. T. Perelman, I. Itzkan, R. R. Dasari, M. S. Feld, *Phys. Rev. Lett.* **1997**, *78*, 1667.
[35] E. C. Le Ru, J. Grand, I. Sow, W. R. C. Somerville, P. G. Etchegoin, M. Treguer-Delapierre, G. Charron, N. Félidj, G. Lévi, J. Aubard, *Nano Lett.* **2011**, *11*, 5013.
[36] S. Nie, S. R. Emory, *Science* **1997**, *275*, 1102.
[37] D. Jimenez De Aberasturi, A. B. Serrano-Montes, J. Langer, M. Henriksen-Lacey, W. J. Parak, L. M. Liz-Marzán, *Chem. Mater.* **2016**, *28*, 6779.
[38] M. Allam, S. Cai, A. F. Coskun, *npj Precis. Onc.* **2020**, *4*, 11.
[39] A. Milewska, V. Zivanovic, V. Merk, U. B. Arnalds, O. E. Sigurjónsson, J. Kneipp, K. Leosson, *Biomed. Opt. Express* **2019**, *10*, 6172.
[40] M. Li, J. Wu, M. Ma, Z. Feng, Z. Mi, P. Rong, D. Liu, *Nanotheranostics* **2019**, *3*, 113.
[41] L. E. Jamieson, S. M. Asiala, K. Gracie, K. Faulds, D. Graham, *Annu. Rev. Anal. Chem.* **2017**, *10*, 415.
[42] E. Lenzi, D. Jimenez De Aberasturi, L. M. Liz-Marzán, *ACS Sens.* **2019**, *4*, 1126.
[43] L. Lin, X. Bi, Y. Gu, F. Wang, J. Ye, *J. Appl. Phys.* **2021**, *129*, 191101.
[44] H. Chen, Z. Cheng, X. Zhou, R. Wang, F. Yu, *Anal. Chem.* **2022**, *94*, 143.
[45] J. C. J. Wei, G. A. Edwards, D. J. Martin, H. Huang, M. L. Crichton, M. A. F. Kendall, *Sci. Rep.* **2017**, *7*, 15885.
[46] M. Khiao In, K. C. Richardson, A. Loewa, S. Hedtrich, S. Kaessmeyer, J. Plendl, *Anat. Histol. Embryol.* **2019**, *48*, 207.
[47] V. K. Kuna, A. M. Padma, J. Håkansson, J. Nygren, R. Sjöback, S. Petronis, S. Sumitran-Holgersson, *Cell Transplant.* **2017**, *26*, 293.
[48] A. M. Lardi, M. Ho-Asjoe, K. Junge, J. Farhadi, *Gland Surg.* **2017**, *6*, 49.
[49] S. Iranpour, N. Mahdavi-Shahri, R. Miri, H. Hasanzadeh, H. R. Bidkhori, H. Naderi-Meshkin, E. Zahabi, M. M. Matin, *Cell Tissue Bank* **2018**, *19*, 357.
[50] N. Kolundzic, P. Khurana, D. Crumrine, A. Celli, T. M. Mauro, D. Ilic, *JID Innov.* **2022**, *2*, 100083.
[51] P. M. Crapo, T. W. Gilbert, S. F. Badylak, *Biomaterials* **2011**, *32*, 3233.
[52] M. T. Wolf, K. A. Daly, E. P. Brennan-Pierce, S. A. Johnson, C. A. Carruthers, A. D'Amore, S. P. Nagarkar, S. S. Velankar, S. F. Badylak, *Biomaterials* **2012**, *33*, 7028.
[53] D. Nasiry, A. R. Khalatbary, M.-A. Abdollahifar, A. Amini, M. Bayat, A. Noori, A. Piryaei, *Arch. Dermatol. Res.* **2021**, *313*, 567.
[54] X. Li, P. Li, C. Wang, T. Shang, H. Han, Y. Tong, Y. Kang, J. Fang, L. A. Cui, *Biomater. Sci.* **2022**, *10*, 2275.
[55] J. López De Andrés, M. Ruiz-Toranzo, C. Antich, C. Chocarro-Wrona, E. López-Ruíz, G. Jiménez, J. A. Marchal, *Biofabrication* **2023**, *15*, 035016.
[56] F. Cardoni, M. Meneghetti, L. Litti, *J. Raman Spectrosc.* **2023**, *55*, 6.
[57] J. M. Mehnert, M. M. McCarthy, L. Jilaveanu, K. T. Flaherty, S. Aziz, R. L. Camp, D. L. Rimm, H. M. Kluger, *Hum. Pathol.* **2010**, *41*, 375.
[58] E. T. Alexander, O. El Naggar, E. Fahey, K. Mariner, J. Donnelly, K. Wolfgang, O. Phanstiel, S. K. Gilmour, *Cancer Biol. Ther.* **2021**, *22*, 225.
[59] O. Shalem, N. E. Sanjana, E. Hartenian, X. Shi, D. A. Scott, T. S. Mikkelsen, D. Heckl, B. L. Ebert, D. E. Root, J. G. Doench, F. Zhang, *Science* **2014**, *343*, 84.
[60] C. Sun, L. Wang, S. Huang, G. J. J. E. Heynen, A. Prahallad, C. Robert, J. Haanen, C. Blank, J. Wesseling, S. M. Willems, D. Zecchin, S. Hobor, P. K. Bajpe, C. Lieftink, C. Mateus, S. Vagner, W. Grernrum, I. Hofland, A. Schlicker, L. F. A. Wessels, R. L. Beijersbergen, A. Bardelli, F. Di Nicolantonio, A. M. M. Eggermont, R. Bernards, *Nature* **2014**, *508*, 118.
[61] J. Tsoi, L. Robert, K. Paraiso, C. Galvan, K. M. Sheu, J. Lay, D. J. L. Wong, M. Atefi, R. Shirazi, X. Wang, D. Braas, C. S. Grasso, N. Palaskas, A. Ribas, T. G. Graeber, *Cancer Cell* **2018**, *33*, 890.
[62] K. Derr, J. Zou, K. Luo, M. J. Song, G. S. Sittampalam, C. Zhou, S. Michael, M. Ferrer, P. Derr, *Tissue Eng. Part C: Methods* **2019**, *25*, 334.

[63] M. Gholipourmalekabadi, M. Mozafari, M. Salehi, A. Seifalian, M. Bandehpour, H. Ghanbarian, A. M. Urbanska, M. Sameni, A. Samadikuchaksaraei, A. M. Seifalian, *Adv. Healthc. Mater.* **2015**, *4*, 918.

[64] M. R. Green, J. Sambrook, *Cold Spring Harb. Protoc.* **2016**, *2016*, pdbprot093377.

[65] H. Yuan, C. G. Khoury, H. Hwang, C. M. Wilson, G. A. Grant, T. Vo-Dinh, T. Gold Nanostars, *Nanotechnology* **2012**, *23*, 075102.